

Influence of Cysteine 440 on the Active Site Properties of 3-Deoxy-D-Arabino-Heptulosonate 7-Phosphate Synthase in *Mycobacterium tuberculosis* (MtDAHPS)

Abayomi S. Faponle,* Bamidele S. Fagbohunka, and James W. Gauld

Cite This: *ACS Omega* 2023, 8, 14401–14409

Read Online

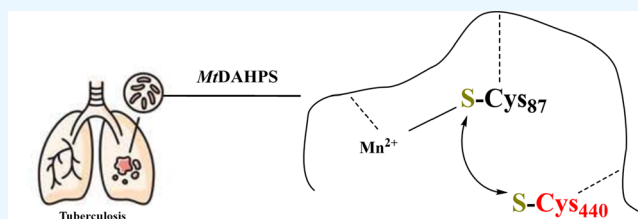
ACCESS |

Metrics & More

Article Recommendations

Supporting Information

ABSTRACT: The shikimate pathway, which produces aromatic amino acids and key intermediates, is critical to the viability of the tuberculosis-causing pathogen *Mycobacterium tuberculosis*. The enzyme 3-deoxy-D-arabino-heptulosonate 7-phosphate synthase (DAHPS) catalyzes the first committed step of this pathway and possesses regulatory functions. Its active site contains two cysteinyls: one (Cys₈₇) bound to a metal ion, while the other (Cys₄₄₀) is in proximity to the first but is located on a connecting loop. This arrangement seemingly appeared as a disulfide linkage. However, Cys₄₄₀ is not metal binding, and its positioning indicates that it could collapse the disulfide linkage. Hence, its potential role may be more than simply structural support of the active site fold. Using a multiscale computational approach, molecular dynamics (MD) simulations, and DFT-based calculations, the influence of Cys₄₄₀ on the active site properties has been investigated. MD simulations reveal an unusually long disulfide bond, more than 3.0 Å, whereas DFT calculations identified two stable active site conformers in the triplet and quintet spin states. Analysis of group spin density distribution identified antiferromagnetic coupling in each conformer, which suggests their relatively low potential energy and stable conformations. The conformer in the triplet spin state could favor enzyme reactivity due to its low HOMO–LUMO energy gap. In addition, reduction of the Cys₄₄₀ thiolate group results in collapse of the active site metal–ligand configuration with large exothermicity. Hence, Cys₄₄₀ could activate and inactivate the enzyme. For the first time, the study revealed the role of Cys₄₄₀ as being vital for the catalytic activity of the enzyme rather than solely for the structural stabilization of its active site. Thus, the findings may lead to a novel basis for antituberculosis drug design and development that would disrupt the contributions of the Cys₄₄₀.

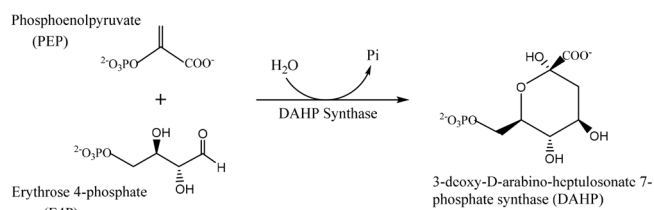


1. INTRODUCTION

Mycobacterium tuberculosis (*Mt*) is the causative agent of tuberculosis, an infectious respiratory system disease that affects millions of people globally.^{1,2} Notably, it utilizes the shikimate pathway to produce aromatic amino acids and important aromatic intermediates. Hence, the unhindered flux of the shikimate pathway is important for the survival and viability of *M. tuberculosis*.³ While this pathway is also present in plants and microorganisms including apicomplexan parasitic organisms^{4,5} it is lacking in humans and other higher animals.⁶ Thus, it is recognized as a key target for the development of antibiotics including antimycobacterial agents.

The enzyme 3-deoxy-D-arabino-heptulosonate 7-phosphate synthase (DAHPS) is vital to the shikimate pathway, as it allosterically regulates the pathway's flux of substrates and products.^{6–10} Furthermore, it catalyzes the first committed step in the pathway: conversion of phosphoenolpyruvate (PEP) and erythrose-4-phosphate (E4P), via an aldol-like condensation reaction, to inorganic phosphate and 3-deoxy-D-arabino-heptulosonate 7-phosphate (Scheme 1). The latter is then converted, via a series of reactions catalyzed by six other enzymes in tandem, to give the key metabolite chorismate,

Scheme 1. Condensation Reaction Catalyzed by DAHP Synthase



from which three aromatic amino acids and other phenolic compounds are derived.⁷

DAHPS has been shown to have at least four possible allosteric regulatory mechanisms. First, these may in part be elicited by the singular and/or separate action of each of the

Received: November 30, 2022

Accepted: March 31, 2023

Published: April 11, 2023



three aromatic amino acids as found, for example, in *E. coli* DAHPS isozymes, whereby activity is feedback inhibited by either phenylalanine, tyrosine, or tryptophan.¹¹ Second, it can involve the synergistic actions of tyrosine and tryptophan and noncovalent association with chorismate mutase in *M. tuberculosis* MtDAHPS.^{12,13} Third, an N-terminal linked ferredoxin-like regulatory domain can help alter the conformation of the substrate-binding channel upon binding of phenylalanine or tyrosine.^{14–16} Lastly, the regulatory activity of a N-terminal linked chorismate mutase-like domain responds to chorismate and prephenate binding.^{17–19} DAHPS members belong to one of the two distinct family types, I and II, which have distinct molecular size and amino acid sequences.^{20,21} More specifically, type I's are smaller than type II, with the former having masses of <40 kDa, whereas the latter have masses >50 kDa. Type I members, while sharing a common (β/α)₈ TIM barrel fold and an additional structural domain relevant for allosteric control,^{10,22} can be further subdivided into type I α and I β sequence subfamilies.

Despite low sequence homology between types I and II, less than 10%, the fold of the monomeric unit, the structural arrangement of key active site residues, substrate binding modes, and divalent metal ions within the catalytic site are similar, thus indicating a common ancestral relationship.²² Type II DAHPS occurs in many disease-causing bacteria and as a result are seen as key drug targets, particularly in developing narrow-spectrum antibacterial agents. MtDAHPS is an example of a type II isozyme,²² and hence, a detailed understanding of the roles of its key active site residues could lead to the design and development of new and targeted antimycobacterial agents.

The active site of MtDAHPS (Figure 1) is dependent on the presence of a divalent metal ion for the catalytic activity. Experimentally, treatment of apo-MtDAHPS with EDTA and various divalent metal ions found Co(II) and Mn(II) most effective at restoring activity to 100% and 76%, respectively.²²

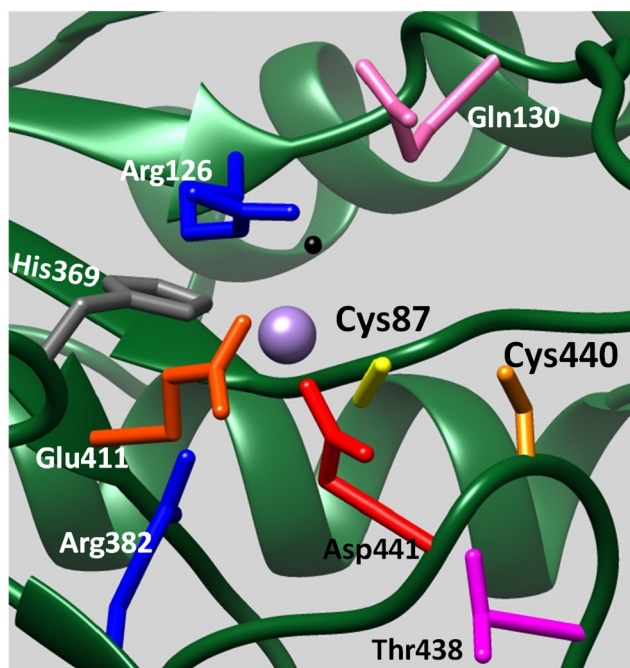


Figure 1. Active site of MtDAHPS. Manganese (purple), oxy atom of water bound to Mn (black) (PDB ID 3NUE).

The metal ion plays a structural role by coordinating key residues to help form an active site catalytic motif, which seems to favor binding of a water molecule for activation.²³ In the native state, Mn(II) is hexacoordinated to the side chains of an aspartyl (Asp₄₄₁), glutamyl (Glu₄₁₁), histidyl (His₃₆₉), and cysteinyl (Cys₈₇), with a water molecule filling the sixth position. Although DAHPS is a transferase, its active site arrangement resembles the motif of many nonheme transition-metal-dependent oxygenases and sulfoxidases that aid oxygen-functionalization of carbon and C–S activation of organic substrates.^{24–27}

However, a unique feature of the MtDAHPS active site is the presence of a second cysteinyl residue (Cys₄₄₀) that is purported to form a disulfide link with the proposed Mn(II)-ligating cysteinyl (Cys₈₇). Unfortunately, it is unclear if this purported disulfide bond is consistent throughout the catalytic mechanism or only transiently formed and at a specific step(s), such as in regulation of metal binding. Furthermore, its possible structural and electronic roles in conferring transferase activity to DAHPS are also unknown.

In this study, we have applied a multiscale computational approach to investigate possible structural and electronic roles and impacts of Cys₄₄₀ on the active site of 3-deoxy-D-arabino-heptulosonate 7-phosphate synthase (DAHPS) from *Mycobacterium tuberculosis* (*Mt*). More specifically, we have used molecular dynamics (MD) simulations and density functional theory (DFT)-based quantum mechanical (QM)-cluster approaches to examine structural and electronic contributions of Cys₄₄₀ to the catalytic site properties of MtDAHPS.

2. RESULTS AND DISCUSSION

As noted in the Introduction, 3-deoxy-D-arabino-heptulosonate 7-phosphate synthase (DAHPS) is the first enzyme of the multienzyme shikimate pathway. More specifically, DAHPS converts phosphoenolpyruvate (PEP) and erythrose-4-phosphate to inorganic phosphate and 3-deoxy-D-arabino-heptulosonate 7-phosphate via a condensation reaction. Importantly, the enzyme fold consists of a catalytic domain and a regulatory domain.¹²

The active site of MtDAHPS has Mn²⁺ ions bound to four residues via their amino acid side chains (with bonding contributions from S(γ) of Cys₈₇, N(ϵ 2) of His₃₆₉, O(ϵ 2) of Glu₄₁₁, and O(δ 2) of Asp₄₁₁), and a water molecule. In addition, Cys₄₄₀ is also positioned in the vicinity of the metal center and is spatially close to the metal–ligand Cys₈₇ resembling a cystine.²² In the setup of the active site, we considered the sixth ligand coordination to the metal center. As such, that position was filled with a water molecule in place of the E4P carbonyl O. Essentially, the water-liganded metal active center represents the starting reactant manifold in the catalytic cycle of the enzyme. We sought to understand the details of this structural complex in this current study.

To investigate the roles of Cys₄₄₀, we performed a series of molecular dynamics (MD) simulations on the full enzyme.

2.1. Molecular Dynamics Simulations of MtDAHPS.

The MD simulations performed can be considered as being of four systems (I, II, III, and IV) which differed only in structural restraints applied:

- I. all key elements of the active site (i.e., Mn²⁺, the four metal-ligated residues (Cys₈₇, Asp₄₁₁, Glu₄₁₁, and His₃₆₉), water ligand, and Cys₄₄₀) were kept restrained for the 40 ns MD simulation;

- II. as for system I, but Asp₄₄₁, Cys₈₇, and Cys₄₄₀ were unrestrained during the MD simulation, which was run for 75 ns;
- III. as for system I, except Cys₄₄₀ was unrestrained over the 40 ns MD simulation; and
- IV. as for system I, except Cys₈₇ and Cys₄₄₀ were unrestrained over the 35 ns MD simulation (see text).

That is, in system I, all key elements of the active site (i.e., the catalytically important Mn²⁺ ion, its four ligated residues Cys₈₇, Asp₄₁₁, Glu₄₁₁, and His₃₆₉, and water), as well as Cys₄₄₀ were held constant. In the other systems (II, III, and IV), one or more selected metal-ligated residues and Cys₄₄₀ were allowed to fluctuate over the course of the MD simulations. The systems I, III, and IV showed similar conformational variability over the course of the MD simulations, with root mean squared deviations (RMSD) in the range between ~ 1.5 and 3.2 Å. Meanwhile, the RMSDs of system II showed great variability lying in the approximate range of ~ 1.5 – 6.0 Å (Figure S1). It is noted that for system II, the longer duration of the MD simulation was in response to the greater variation in RMSD to help ensure it was not an artifact of an unequilibrated system (see Figure 2).

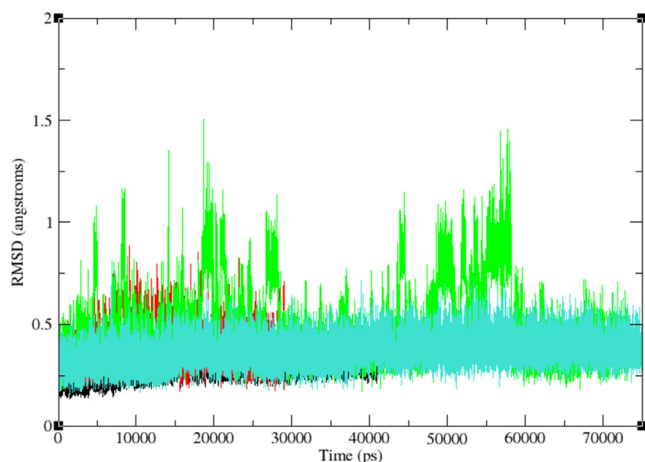


Figure 2. Plots of the root-mean-square deviation (RMSD) values obtained for the Asp₄₄₁, Cys₈₇, and Cys₄₄₀ residues in systems I (black), II (green), III (turquoise blue), and IV (red).

The conformational variability in II could, in part, be due to the large but flexible domains of the protein fold. However, to focus on the region that is relevant to the study, RMSD plots of the three key residues Asp₄₄₁, Cys₈₇, and Cys₄₄₀ in the four MD simulations were obtained and are shown in Figure 2. The largest variation (RMSD range: ~ 0.23 – 1.5 Å) in the plots due to conformational fluctuations of the three residues was observed in the MD simulation on system II (green). Although it appeared that the fluctuation was similar to that by IV (red), a critical observation of the structure over the course of the simulations revealed the trailing pattern was conferred by only the Cys₄₄₀ but the metal-S(γ) (of Cys₈₇) bond distance was maintained all the time (Figure S2) and so the simulations of IV were discontinued at 35 ns.

Focus was then placed on the dynamic behavior observed for system II. To help identify the key residues responsible for the large conformational variability observed, RMSD values of the Asp₄₄₁ and Cys₄₄₀ residues for all four systems were plotted and are shown in Figure 3. These clearly illustrate that the fluctuations are due to the presence of Asp₄₄₁ and Cys₄₄₀. However, the differences in observed RMSD value ranges, i.e., 0.00 to ~ 1.53 Å for Asp₄₄₁ (Figure 3A) versus 0.00 to ~ 0.79 Å for Cys₄₄₀ (Figure 3B) indicate that the fluxionality of Cys₄₄₀ is dependent on Asp₄₄₁, even as the Asp₄₄₁ O($\delta 2$) center remained bonded to the metal site during the course of the MD simulations. This dependence may not be unconnected to the location of the two residues; both are located on the connecting loop between the β -strand and α -helices in the C-terminally situated active site.²² It was observed that this connecting loop maintained its fold over the course of the MD simulations and, thus, contributes to the preservation of the structural integrity of the active site.

For specific analysis of the MD simulations trajectory of II, its RMSD plots revealed only two residues; Asp₄₄₁ and Cys₄₄₀ exhibited apparently large conformational variability, therefore eliminating the contributions of Cys₈₇, whose structural role seems to be coordination to the metal site for catalytic function, because of the observed conformational convergence throughout the period of the simulations (Figure 4a). In addition, for visual inspections of the positions of the atoms, four conformations (pdb) were sampled along the MD trajectory whereby snapshots (pdb frames) taken at 10, 30, and 70 ns were overlaid on the equilibrated structure (Figure 4b). It is obvious that although most amino acid residues

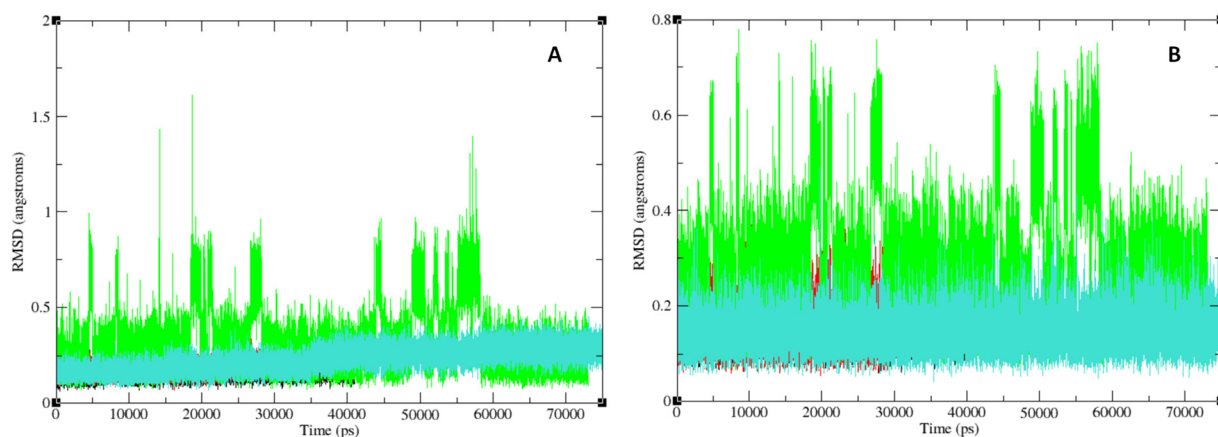


Figure 3. Plots of the RMSD values obtained for only the (A) Asp₄₄₁ and (B) Cys₄₄₀ residues during the MD simulations on systems I (black), II (green), III (turquoise blue), and IV (red).

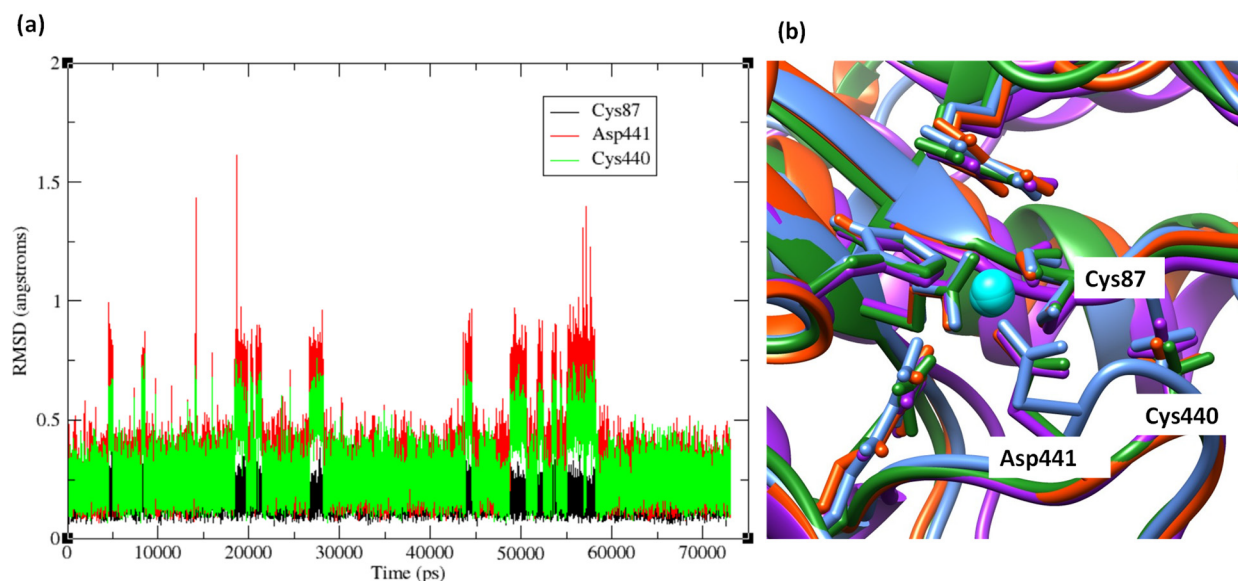


Figure 4. (a) RMSD plots of Cys₈₇, Asp₄₄₁, and Cys₄₄₀ residues of MD simulations in which the three amino acid residues were not constrained for 75 ns (II); (b) overlay of the initial equilibrated structure (purple) and snapshots of the MD trajectory at 10 ns (red), 30 ns (blue), and 70 ns (green) of *MtDAHPS*. Mn(II) ion (cyan).

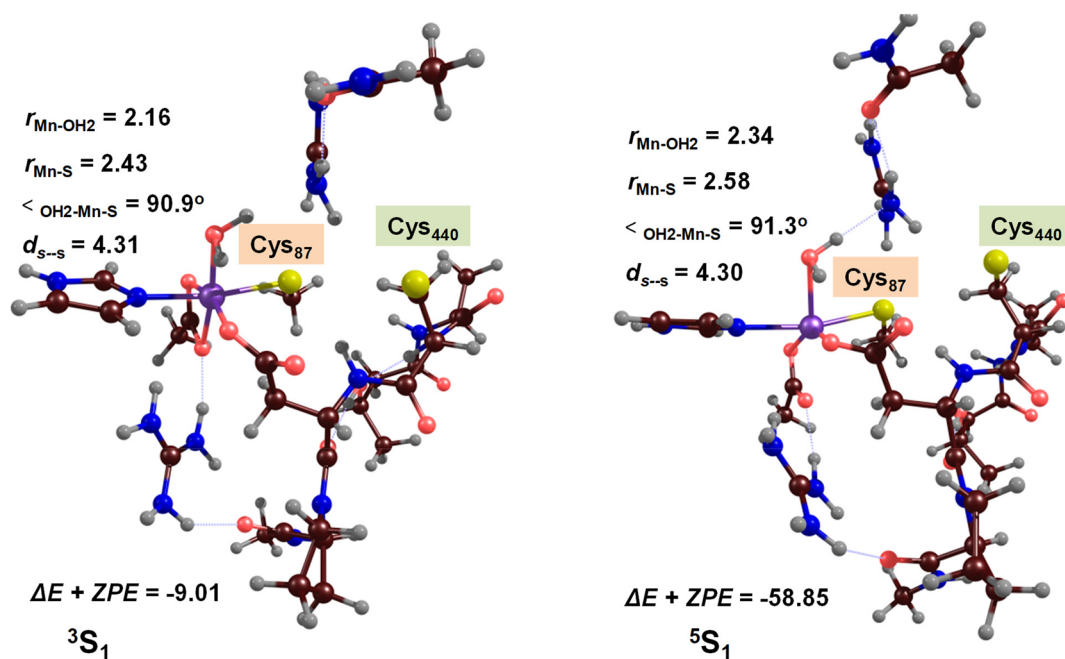


Figure 5. Optimized geometries of low-lying spin states of the metal-coordinated active site atoms of *MtDAPHs* as obtained at the UB3LYP/BS1//BS2 level of theory. Bond lengths are in angstroms (Å), and energy is in kcal mol⁻¹. ZPE: zero-point energy correction. Atom labels are S (yellow), Mn (purple), C (dark brown), H (gray), O (red), and N (blue).

within the second coordination environment of the active site metal site were not constrained except Cys₄₄₀, they did not deviate considerably from their initial positions. Of course, among the metal-coordinating residues, only Asp₄₄₁ and Cys₈₇ were allowed to move, but it can be seen in Figure 4b that Cys₈₇ and Asp₄₄₁ (for Asp₄₄₁, regardless of movements of side chain) remained bound to the metal ion, Mn²⁺, whereas Cys₄₄₀ changes positions several times, thus adjusting the Cys₈₇(Sγ)⋯Sγ(Cys₄₄₀), i.e., S–S, distances.

In addition to the four conformations discussed above, five more snapshots (at 19, 25, 27, 40, and 60 ns) were sampled. In all, the S–S distance ranges between 3.24 and 4.92 Å, with

~3.60 Å within the equilibrated structure and 4.14 Å in pdb at 70 ns. These S–S distances are somewhat longer than the typical range of 2.0–3.0 Å in disulfide bonds found in most proteins and peptides.^{37–40} Moreover, either the torsion angles (Cβ–Sγ–Sγ–Cβ) or the Cβ(of Cys₈₇)-Sγ–Sγ/Cβ(of Cys₄₄₀)-Sγ–Sγ angles, which measured approximately -4.1°, -8.5°, -45.5°, -6.1° or 116.4°/76.6°, 123.4°/83.4°, 131.0°/76.7°, 121.2°/78.4° found within the conformations of equilibrated structure, and those at 10, 30, and 70 ns, respectively, deviate from optimal values for cystinyl disulfides of proteins and peptides. It has been reported that even slight deviation from the optimal values is associated with energy cost by several kcal

mol^{-1} as the torsion angle is critical for the stability of a disulfide bond.⁴¹

Surprisingly, the varying S–S distance of the Cys₈₇–Cys₄₄₀, which leads to deviation from optimal characteristics of a usual cystine, did not lead to structural collapse of the metal-containing active site architecture. It is obvious that the positioning of Cys₄₄₀ is strategic, and its roles, possibly, could be beyond structural stabilization of the active site. As such, we suggest Cys₄₄₀ could be an actual participant in the catalytic function of the enzyme, whereby its contributions are at the quantum chemical or electronic level. Hence, to investigate its quantum chemical contributions, QM (DFT), calculations on the active site cluster model.

2.2. DFT Studies of MtDAHPS. A cluster model of the active site was obtained at 1.2 ns in the MD simulation on system I. The connecting loop, which bears Cy₄₄₀ but consists of the pentapeptide, Pro₄₄₂–Asp₄₄₁–Cys₄₄₀–Ala₄₃₉–Thr₄₃₈, was included in the model in order to retain the fold as in the pdb (see Computational Methods). To investigate the quantum chemical contributions of Cys₄₄₀, we performed geometry optimizations, geometry scans, and analytical frequency calculations on the active site model of MtDAHPS. Geometry optimizations were done at singlet, triplet, and quintet spin states on the QM atoms at the unrestricted hybrid UB3LYP/BS1//BS2 level of theory, which gave the structures ¹S₁, ³S₁, and ⁵S₁, respectively. The B3LYP method has been reported several times to be successful on transition metal-containing metalloenzymes.⁴² The relative energies and subsequent results calculated for the three structures revealed a high energy path for ¹S₁, therefore, we will focus on ³S₁ and ⁵S₁ (Figure 5). The ³S₁ and ⁵S₁ states have relative energies $\Delta E + \text{ZPE}$ of -9.01 and -58.85 kcal mol⁻¹, respectively. Although these values suggest that structures ³S₁ and ⁵S₁ are relatively stable, the energy gap between them is quite large at -49.84 kcal mol⁻¹. Interestingly, the quintet high-spin ground state found for the water-ligated manganese(II) complex is consistent with theoretical and experimental studies that involve biomimetic nonheme manganese and manganese-porphyrinoid complexes.^{45–49}

Comparably, there are subtle differences in the geometric properties of the two structures. For instance, the Mn–water bond lengths, $r_{\text{Mn-OH}_2}$, are 2.16 and 2.34 Å in ³S₁ and ⁵S₁, respectively, and the Mn–S distance is 2.43 Å in the former and 2.58 Å in the latter. Nonetheless, similar bond lengths were found in enzymes that have Sy of cysteinyl ligand to the metal center.^{26,27,43,44} The water molecule is bound at $\sim 90^\circ$ in both spin states. These geometric characteristics are not dramatically different and do not seem to account for the large energy gap of the low-lying states of the two structures. Thus, we suggested the energy difference might be occasioned by the electronic distribution pattern of each geometric state. Nonetheless, before we probed further, we did geometric scans of several atoms in an effort to search for global and local minima including transition states, i.e., probable reaction pathways that may emanate from the stable structures, ³S₁ and ⁵S₁.

The three geometric scans involved stepwise reduction of bond distances between the target atoms and, therefore, were between (1) S γ atoms of Cys₄₄₀ and Cy₈₇, (2) N β (peptide bonds) of Asp₄₄₁ and the S γ atom of Cys₄₄₀, (3) the amide H atom of Asp₄₄₁ and the S γ atom of Cys₄₄₀ on the three low-lying spin states, singlet, triplet, and quintet. Each geometric

coordinate in 2 and 3 followed a high energy path that gave no candidates for the transition-state structure and energy search. By contrast, only in 1 did the scan follow a lower energy path and only on the triplet and quintet spin surfaces (Figure S3). Geometric optimization of structures at the lower end of the energy troughs results in a new conformer, S₂, that is much lower in energy, $\Delta E + \text{ZPE} = -32.84$ kcal mol⁻¹, on the triplet spin surface, ³S₂, and another lower-energy conformer, ⁵S₂, relative to S₁ (Figure 6). Note that the S–S distance had been

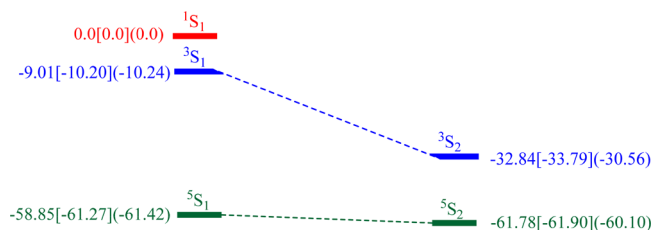


Figure 6. Potential energy landscape of two active site conformers of MtDAHPS in the low-lying spin states. Relative energies are in the format $\Delta E + \text{ZPE}[\Delta G](\Delta E_{\text{BS}2} + \text{ZPE})$ in kcal mol⁻¹ as obtained at the UB3LYP/BS1//BS2 level of theory.

reduced from 4.30 Å in S₁ to 3.12–3.13 Å in S₂ conformers, which are 0.12–0.13 Å longer than the usual 2.0–3.0 Å found for reversible and structural disulfides.^{37–40} In fact, two conformers, ³S₂ and ⁵S₁, are implicated, which could be related to the results of the MD simulations discussed earlier, *vide supra*, whereby the S γ –S γ distance adjusts values within different conformational states.

Furthermore, as shown in Figure 7, small but not dramatic changes were observed in ³S₂ and that include the Mn–OH₂ bond length which had increased by 0.2 to 2.36 Å and a

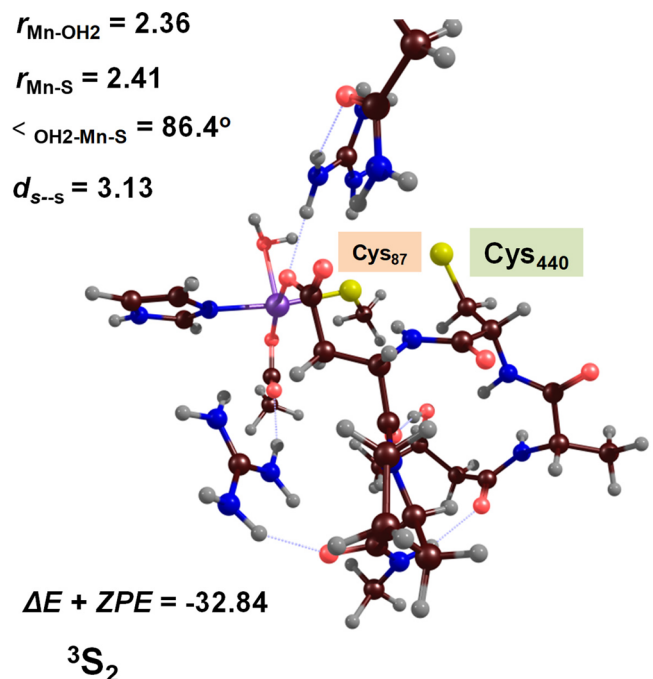


Figure 7. Optimized geometry of an active site conformer, ³S₂, of MtDAHPS as obtained at the UB3LYP/BS1//BS2 level of theory. Bond lengths are in angstroms (Å) and energy in kcal mol⁻¹. ZPE: zero-point energy correction. Atom labels are S (yellow), Mn (purple), C (dark brown), H (gray), O (red), and N (blue).

decrease in H₂O–Mn–S angle from 90° to 86.4° because of the stretched Mn–OH₂ bond length. The Mn–S bond length of 2.4 Å remained intact. Importantly, the question here is what could be the origin of the geometric stabilization of these conformers? Hence, analysis of the group spin densities and molecular orbital occupations of the electrons in the conformers revealed an interesting result.

In Table S3, the details of the group spin densities of S₁ and S₂ in the low-lying spin states are given. Here, we will summarize the most relevant spin densities distributions. In ³S₁ and ⁵S₁ there were spin densities of 1.07 (α) and 4.82 (α) on Mn(II), and 0.93 (α) and 0.95 (β) on the cysteinyl group (Cys₄₄₀) mostly localized on the thiolate group, respectively. Redistribution of these spin densities had occurred in ³S₂ and ⁵S₂ such that Mn(II) now bears 2.99 and 4.76 α and then 0.79 and 0.76 β on the Cys₄₄₀ atoms. Note that α/β is up-spin/down-spin electrons. Interestingly, while β-spins of the Cys₄₄₀ group remained antiferromagnetically coupled to α-spins of Mn(II) in both ⁵S₁ and ⁵S₂ conformers, which makes them lower-energy conformers, the α-spins of Cys₄₄₀ in ³S₁ turned to β-spins in ³S₂, resulting in antiferromagnetic coupling to the metal 3d unpaired electrons, which is suggested to have caused a sudden drop in electronic energy and made the second conformer, ³S₂, stable.

Furthermore, the orbital occupation of ⁵S₁ is $\pi_{xy}^2 \pi_{yz}^1 \sigma_{x^2-y^2}^* - y^2$ $\sigma_{z^2}^* \pi_{z, Cys440}^1$ in the quintet spin state, whereas that of ³S₂ is $\pi_{xy}^2 \sigma_{z^2}^* \sigma_{x^2-y^2}^* - y^2$ $\pi_{z, Cys440}^1$ in the triplet spin state. In ⁵S₁, the metal 3d orbital mixed less with the surrounding atomic orbital of the metal–ligands, but more mixing was seen in the ³S₂, particularly along the metal–Sγ(Cys₈₇)-Sγ(Cys₄₄₀) axis by $\sigma_{z^2}^*$ and $\sigma_{x^2-y^2}^*$ orbital (Figures S4 and S5). The molecular orbital $\sigma_{z^2}^*$ and $\sigma_{x^2-y^2}^*$ are ordered in a way that $\sigma_{x^2-y^2}^*$ is singly occupied before $\sigma_{z^2}^*$ in the quintet spin state and vice versa in the triplet spin state, even as the latter carried two electrons. Specifically, the difference in energy of the HOMO–LUMO gap between the two spin states is 11.66 kcal mol⁻¹ in favor of ³S₂. These differences in molecular orbital interactions and orbital ordering might contribute to the energy gap between ⁵S₁ and ³S₂ and, consequently, could determine chemical reactivity in the enzyme subsequent reactions. These results pointed to the significance of the contributions of electronic distributions in the conformers with respect to spin-state preference and molecular orbital interactions with consequent antiferromagnetic coupling of electrons (spins) of key atoms in the active site, which led to the most preferred low-energy conformer and spin state in the ground state. The current study presents the first study of the intricate details of the thiolate interaction between two cysteinyl residues within the active site of MtDAHPS.

Lastly we examined the reduction of Cys₄₄₀. By adding a hydrogen atom to the Sγ atoms of ^{3,5}S, the active site configurations drastically became destabilized with most of the metal–ligand coordination lost in both triplet and quintet spin states. Thermochemical calculations of the (destabilization/inactivation) reactions indicated a large exothermicity, –144.49 kcal mol⁻¹ and –129.15 kcal mol⁻¹ for ³S and ⁵S, respectively, with the water molecule completely detached in the quintet spin state. This suggests that an oxidized Cys₄₄₀ is required for maintaining the enzyme activity and a reduced Cys₄₄₀ would cause the enzyme to lose activity, which contrasts the proposition of Webby et al. that the enzyme was

inactivated under oxidizing conditions by forming a disulfide bond between the two cysteinyl groups.²²

3. CONCLUSIONS

In this study, a multiscale computational approach has been applied to investigate the influence of Cys₄₄₀ uniquely present in the active site fold of DAHPS from *Mycobacterium tuberculosis*, MtDAHPS. This approach includes the application of molecular dynamics (MD) simulations to the full enzyme as well as density functional theory (DFT) calculations to a QM-cluster model of the enzyme's active site.

The results of the MD simulations revealed the dynamic behavior of thiolate group of Cys₄₄₀ toward the thiolate of Cys₈₇ involved in metal binding. Importantly, on an intermittent basis, the Sγ(Cys₄₄₀) was brought into the S–S distance that resembles a disulfide, although with distances above 3.0 Å, the upper value for the structural disulfide bond. Despite the ranging S–S distance occasioned by the Cys₄₄₀ manifold, the structural configuration of the metal–ligand active site remained intact. These results suggested that Cys₄₄₀ positioning makes it possible to contribute at the electronic level to the energetics of the enzyme reaction and enzyme activation–inactivation, as evident by subsequent quantum chemical calculations.

In addition, the DFT results revealed two energetically stable conformers on the triplet and quintet spin surfaces. An antiferromagnetic coupling of the Sγ electron to the 3d metal electrons found in both conformers is suggested to have contributed to their relative stability. Although the two conformers are proposed to be able to initiate chemical reactivity in the enzyme, it is more likely to proceed faster on the triplet spin state since a HOMO–LUMO gap of 11.66 kcal mol⁻¹ was found to be in favor of the conformer on the triplet spin state.

Furthermore, reduction of the thiolate group of Cys₄₄₀ by addition of a hydrogen atom resulted in destabilization of the metal–ligand active site fold, which, in fact, led to release of metal-bound water molecules and reduction in metal–ligand coordination of key residues in the triplet and quintet spin states. These results indicated that the enzyme is inactivated once Cys₄₄₀ is reduced and activated when it is oxidized. The current study presents the first study of the intricate details of thiolate interaction between two cysteinyl residues within the active site of MtDAHPS. This also revealed, for the first time, that disulfide link formation between the metal–liganded cysteine (Cys₈₇) and the proximal cysteine (Cys₄₄₀) was not important but that the thiolate group of Cys₄₄₀ is required to energy stabilize the ground state reactant. Thus, revealing the role of Cys₄₄₀ being vital for the catalytic activity of the enzyme rather than solely for structural stabilization of its active site. The findings may lead to a novel basis for antituberculosis drug design and development that would disrupt the contributions of the Cys₄₄₀.

Finally, we conclude that the presence of Cys₄₄₀ in MtDAHPS confers vital structural and electronic properties to its active site which, consequently, would determine enzyme reactivity and, also, whether the enzyme is active or inactive dependent on the oxidation–reduction state of the thiolate group of Cys₄₄₀. Importantly, this study has provided detailed understanding of the roles of a vital active site residue and, thus, provides a prospect for drug discovery that targets this residue in the fight against tuberculosis.

4. COMPUTATIONAL METHODS

In order to unravel the role that Cys₄₄₀ plays in the active site of MtDAHPS, we performed both molecular dynamics (MD) simulations and QM-cluster density functional calculations of the enzymes. Details of these computational methods were outlined in our previous work^{27,28} that focused on enzymes. Thus, herein, only succinct descriptions of the methods used in this study are highlighted. All DFT calculations and MD simulations were performed using Gaussian09²⁹ and AMBER16,³⁰ respectively.

4.1. Molecular Dynamics Simulations. A suitable X-ray crystal structure (PDB ID 3NUE) of the enzyme with a 2.50 Å resolution was obtained from the protein data bank repository.¹² Using the H++ Web server,³¹ the protein was protonated at pH 7.0. For the titratable amino acid residues, arginyls and lysyls were protonated, while glutamyls and aspartyls were chosen to be in their deprotonated (i.e., negative charge) states. Of the histidyls, 12 were neutral, singly protonated at N δ (His_{198,369,409}) or N ϵ -(His_{164,195,277,292,326,341,373,383,398}), while four (His_{98,247,359,404}) were charged, i.e., protonated at both N δ and N ϵ . Consequently, the overall charge of the system is -9 . Parameterization of the active site, using the metal center parameter builder (mcpb.py version) in ambertools,³² was done following its geometry optimization and electrostatic potential charge fitting with Gaussian09 at the UB3LYP^{33,34}/BS1 level of theory (BS1:6-31G(d)³⁵ on all atoms except Mn, which has the LANL2DZ ECP³⁶ basis set). The TIP3 water model was used for explicit solvation of the system which was immersed in a truncated octahedron waterbox of radius 14 Å. The solvated system was then made charge neutral by adding nine sodium ions. A water molecule bound to the Mn was retained and was part of the active site in all calculations. Therefore, the entire system consisted of 49 222 atoms, which included 14 045 molecules of TIP3 water model. A series of minimization steps were performed on the solvated system: (i) hydrogen atoms on heavy atoms with the SHAKE algorithm; (ii) the protein backbone; and (iii) all heavy atoms except the active site metal–ligand residues. Next, solvent water molecules were energy-minimized, and the temperature was raised to 300 K by heating using Langevin dynamics with the collision frequency γ_{In_2} , at a constant pressure and with periodic boundary conditions ($n_{tp} = 1$). Finally, all atoms except those of the key active site residues, which were restrained, were minimized. The whole solvated system was then submitted for a 40 or 75 ns production MD simulation, after equilibration, and the structures sampled were analyzed to select a suitable structural template for subsequent DFT calculations.

4.2. DFT Calculations. A suitable structure for constructing the QM-cluster model was obtained from the 1.2 ns snapshot in the MD simulation. The resulting QM-cluster consisted of the Mn(II) ion and models of the residues to which it is ligated: the imidazole of His₃₆₉, methyl carboxylic moieties of Glu₄₁₁ and Asp₄₄₁, the methyl sulfide moiety of Cys₈₇, and a water molecule. In addition, contributions from the second coordination sphere of the Mn(II) were also included: the guanidino moieties of Arg₁₂₆ and Arg₃₈₂, the acetamide moiety of Gln₁₃₀, and a pentapeptide unit (Pro₄₄₂-Asp₄₄₁-Cys₄₄₀-Ala₄₃₉-Thr₄₃₈). In total the system consisted of 119 atoms. All geometry optimizations were performed at the UB3LYP/BS1 level of theory and on the singlet, triplet, and

quintet spin states. The general polarity of the surrounding environment was modeled using the default integral equation formalism polarized continuum (IEFPCM) solvation model in Gaussian 09²⁹ with a dielectric constant (ϵ) of 4.24. Harmonic vibrational frequencies were obtained for all optimized structures to also confirm that they were all energy minima. Relative energies were obtained by performing single-point calculations on the above optimized structures at the UB3LYP/BS2 level of theory (BS2:6-311+G* on all atoms except Mn which has the LANL ECP). It is noted that several geometry scans were performed on initial optimized structures at each spin state to explore the potential energy surfaces between the optimized structures.

■ ASSOCIATED CONTENT

Supporting Information

The Supporting Information is available free of charge at <https://pubs.acs.org/doi/10.1021/acsomega.2c07662>.

rmsd plots of proteins, absolute and relative energies, spin densities, mulliken charges of all optimized geometries, geometry scan profiles, molecular orbital occupations, and atomic Cartesian coordinates (PDF)

■ AUTHOR INFORMATION

Corresponding Author

Abayomi S. Faponle – Department of Biochemistry, Faculty of Basic Medical Sciences, Olabisi Onabanjo University, Ago-Iwoye 120107, Nigeria; orcid.org/0000-0002-6989-0342; Email: asfb340@yahoo.com

Authors

Bamidele S. Fagbohunka – Department of Biochemistry, Faculty of Basic Medical Sciences, Olabisi Onabanjo University, Ago-Iwoye 120107, Nigeria

James W. Gauld – Department of Chemistry and Biochemistry, University of Windsor, Windsor, Ontario N9B 3P4, Canada; orcid.org/0000-0002-2956-9781

Complete contact information is available at:

<https://pubs.acs.org/doi/10.1021/acsomega.2c07662>

Author Contributions

Abayomi S. Faponle: molecular dynamics simulations, density functional calculations, analyses, and writing; Bamidele S. Fagbohunka: molecular dynamics simulations; James W. Gauld: writing and editing.

Notes

The authors declare no competing financial interest.

■ ACKNOWLEDGMENTS

We thank the Natural Science and Engineering Research Council of Canada (NSERC) for financial support. We thank Digital Research Alliance for computational resources.

■ REFERENCES

- Stokstad, E. Infectious disease: drug-resistant TB on the rise. *Science* **2000**, *287*, 2391.
- Tuberculosis (TB). World Health Organization (WHO), October 14, 2021. <https://www.who.int/news-room/fact-sheets/detail/tuberculosis> (accessed 2022-06-22).
- Parish, T.; Stoker, N. G. The common aromatic amino acid biosynthesis pathway is essential in *Mycobacterium tuberculosis*. *Microbiology* **2002**, *148*, 3069–3077.

- (4) Roberts, F.; Roberts, C. W.; Johnson, J. J.; Kyle, D. E.; Krell, T.; Coggins, J. R.; Coombs, G. H.; Milhous, W. K.; Tzipori, S.; Ferguson, D. J. P.; Chakrabarti, D.; McLeod, R. Evidence for the shikimate pathway in apicomplexan parasites. *Nature* **1998**, *393*, 801–805.
- (5) Campbell, S. A.; Richards, T. A.; Mui, E. J.; Samuel, B. U.; Coggins, J. R.; McLeod, R.; Roberts, C. W. A complete shikimate pathway in *Toxoplasma gondii*: an ancient eukaryotic innovation. *Int. J. Parasitol.* **2004**, *34*, 5–13.
- (6) Tzin, V.; Galili, G.; Aharoni, A. Shikimate Pathway and Aromatic Amino Acid Biosynthesis. In *Encyclopedia of Life Sciences*; John Wiley & Sons, 2012.
- (7) Herrmann, K. M.; Weaver, L. M. The Shikimate Pathway. *Annual Review of Plant Physiology and Plant Molecular Biology* **1999**, *50*, 473–503.
- (8) Schoner, R.; Herrmann, K. M. 3-Deoxy-D-arabino-heptulosonate 7-phosphate synthase. Purification, properties, and kinetics of the tyrosine-sensitive isoenzyme from *Escherichia coli*. *J. Biol. Chem.* **1976**, *251*, 5440–7.
- (9) McCandliss, R. J.; Poling, M. D.; Herrmann, K. M. 3-Deoxy-D-arabino-heptulosonate 7-phosphate synthase. Purification and molecular characterization of the phenylalanine-sensitive isoenzyme from *Escherichia coli*. *J. Biol. Chem.* **1978**, *253*, 4259–65.
- (10) Jiao, W.; Blackmore, N. J.; Nazmi, A. R.; Parker, E. J. Quaternary structure is an essential component that contributes to the sophisticated allosteric regulation mechanism in a key enzyme from *Mycobacterium tuberculosis*. *PLoS One* **2017**, *12*, e0180052.
- (11) Shumilin, I. A.; Zhao, C.; Bauerle, R.; Kretsinger, R. H. Allosteric inhibition of 3-deoxy-D-arabino-heptulosonate-7-phosphate synthase alters the coordination of both substrates. *J. Mol. Biol.* **2002**, *320*, 1147–1156.
- (12) Webby, C. J.; Jiao, W.; Hutton, R. D.; Blackmore, N. J.; Baker, H. M.; Baker, E. N.; Jameson, G. B.; Parker, E. J. Synergistic allostery, a sophisticated regulatory network for the control of aromatic amino acid biosynthesis in *Mycobacterium tuberculosis*. *J. Biol. Chem.* **2010**, *285*, 30567–30576.
- (13) Sasso, S.; Okvist, M.; Roderer, K.; Gamper, M.; Codoni, G.; Krengel, U.; Kast, P. Structure and function of a complex between chorismate mutase and DAHP synthase: efficiency boost for the junior partner. *EMBO J.* **2009**, *28*, 2128–2142.
- (14) Wu, J.; Howe, D. L.; Woodard, R. W. *Thermotoga maritima* 3-deoxy-d-arabino-heptulosonate 7-phosphate (DAHP) synthase: the ancestral eubacterial DAHP synthase? *J. Biol. Chem.* **2003**, *278*, 27525–27531.
- (15) Shumilin, I. A.; Bauerle, R.; Wu, J.; Woodard, R. W.; Kretsinger, R. H. Crystal structure of the reaction complex of 3-deoxy-d-arabino-heptulosonate-7-phosphate synthase from *Thermotoga maritima* refines the catalytic mechanism and indicates a new mechanism of allosteric regulation. *J. Mol. Biol.* **2004**, *341*, 455–466.
- (16) Cross, P. J.; Dobson, R. C.; Patchett, M. L.; Parker, E. J. Tyrosine latching of a regulatory gate affords allosteric control of aromatic amino acid biosynthesis. *J. Biol. Chem.* **2011**, *286*, 10216–10224.
- (17) Wu, J.; Sheflyan, G. Y.; Woodard, R. W. *Bacillus subtilis* 3-deoxy-d-arabino-heptulosonate 7-phosphate synthase revisited: resolution of two long-standing enigmas. *Biochem. J.* **2005**, *390*, 583–590.
- (18) Wu, J.; Woodard, R. W. New insights into the evolutionary links relating to the 3-deoxy-d-arabino-heptulosonate 7-phosphate synthase subfamilies. *J. Biol. Chem.* **2006**, *281*, 4042–4048.
- (19) Light, S. H.; Halavaty, A. S.; Minasov, G.; Shuvalova, L.; Anderson, W. F. Structural analysis of a 3-deoxy-D-arabino-heptulosonate 7-phosphate synthase with an N-terminal chorismate mutase-like regulatory domain. *Protein Sci.* **2012**, *21*, 887–95.
- (20) Walker, G. E.; Dunbar, B.; Hunter, I. S.; Nimmo, H. G.; Coggins, J. R. Evidence for a novel class of microbial 3-deoxy-D-arabino-heptulosonate-7-phosphate synthase in *Streptomyces coelicolor* A3(2), *Streptomyces rimosus* and *Neurospora crassa*. *Microbiology* **1996**, *142*, 1973–1982.
- (21) Jensen, R. A.; Xie, G.; Calhoun, D. H.; Bonner, C. A. The correct phylogenetic relationship of KdsA (3-deoxy-D-mannooctulosonate 8-phosphate synthase) with one of two independently evolved classes of AroA (3-deoxy-D-arabino-heptulosonate 7-phosphate synthase). *J. Mol. Evol.* **2002**, *54*, 416–423.
- (22) Webby, C. J.; Baker, H. M.; Lott, J. S.; Baker, E. N.; Parker, E. J. The structure of 3-deoxy-d-arabino-heptulosonate 7-phosphate synthase from *Mycobacterium tuberculosis* reveals a common catalytic scaffold and ancestry for type I and type II enzymes. *J. Mol. Biol.* **2005**, *354* (4), 927–39.
- (23) Furdul, C.; Zhou, L.; Woodard, R. W.; Anderson, K. S. Insights into the mechanism of 3-deoxy-D-arabino-heptulosonate 7-phosphate synthase (Phe) from *Escherichia coli* using a transient kinetic analysis. *J. Biol. Chem.* **2004**, *279* (44), 45618–25.
- (24) Solomon, E. I.; Brunold, T. C.; Davis, M. I.; Kemsley, J. N.; Lee, S.-K.; Lehnert, N.; Neese, F.; Skulan, A. J.; Yang, Y.-S.; Zhou, J. Geometric and Electronic Structure/Function Correlations in Non-Heme Iron Enzymes. *Chem. Rev.* **2000**, *100*, 235–349.
- (25) Costas, M.; Mehn, M. P.; Jensen, M. P.; Que, L., Jr. Dioxygen activation at mononuclear nonheme iron active sites: enzymes, models, and intermediates. *Chem. Rev.* **2004**, *104* (2), 939–86.
- (26) Fellner, M.; Siakkou, E.; Faponle, A. S.; Tchesnokov, E. P.; de Visser, S. P.; Wilbanks, S. M.; Jameson, G. N. L. Influence of cysteine 164 on active site structure in rat cysteine dioxygenase. *J. Biol. Inorg. Chem.* **2016**, *21*, 501–510.
- (27) Faponle, A. S.; Seebeck, F. P.; de Visser, S. P. Sulfoxide Synthase versus Cysteine Dioxygenase Reactivity in a Nonheme Iron Enzyme. *J. Am. Chem. Soc.* **2017**, *139* (27), 9259–9270.
- (28) Faponle, A. S.; Roy, A.; Adelegan, A. A.; Gauld, J. W. Molecular Dynamics Simulations of a Cytochrome P450 from *Tepidiphilus thermophilus* (P450-TT) Reveal How Its Substrate-Binding Channel Opens. *Molecules* **2021**, *26*, 3614.
- (29) Frisch, M. J.; Trucks, G. W.; Schlegel, H. B.; Scuseria, G. E.; Robb, M. A.; Cheeseman, J. R.; Scalmani, G.; Barone, V.; Petersson, G. A.; Nakatsuji, H.; et al. *Gaussian*; Gaussian, Inc.: Wallingford CT, 2016.
- (30) Case, D. A.; Betz, R. M.; Cerutti, D. S.; Cheatham, T. E., III; Darden, T. A.; Duke, R. E.; Giese, T. J.; Gohlke, H.; Goetz, A. W.; Homeyer, N.; et al. *AMBER 2016*; University of California, San Francisco, 2016.
- (31) Anandakrishnan, R.; Aguilar, B.; Onufriev, A. V. H++ 3.0: Automating pK prediction and the preparation of biomolecular structures for atomistic molecular modeling and simulations. *Nucleic Acids Res.* **2012**, *40*, W537–W541.
- (32) Li, P.; Merz, K. M., Jr. MCPB.py: A python based metal center parameter builder. *J. Chem. Inf. Model.* **2016**, *56*, 599–604.
- (33) Becke, A. Density-functional thermochemistry. III. The role of exact exchange. *J. Chem. Phys.* **1993**, *98*, 5648.
- (34) Lee, C.; Yang, W.; Parr, R. G. Development of the Colle-Salvetti correlation-energy formula into a functional of the electron density. *Phys. Rev. B* **1988**, *37*, 785.
- (35) Hehre, W. J.; Ditchfield, R.; Pople, J. A. Self-Consistent molecular orbital methods. XII. Further extensions of Gaussian—Type basis sets for use in molecular orbital studies of organic molecules. *J. Chem. Phys.* **1972**, *56*, 2257–2261.
- (36) Hay, P. J.; Wadt, W. R. Ab initio effective core potentials for molecular calculations. Potentials for the transition metal atoms Sc to Hg. *J. Chem. Phys.* **1985**, *82*, 270–283.
- (37) Wiedemann, C.; Kumar, A.; Lang, A.; Ohlenschläger, O. Cysteines and Disulfide Bonds as Structure-Forming Units: Insights From Different Domains of Life and the Potential for Characterization by NMR. *Front. Chem.* **2020**, *8*, 280.
- (38) Sun, M. A.; Wang, Y.; Zhang, Q.; Xia, Y.; Ge, W.; Guo, D. Prediction of reversible disulfide based on features from local structural signatures. *BMC Genomics* **2017**, *18*, 279.
- (39) Dombkowski, A. A.; Sultana, K. Z.; Craig, D. B. Protein disulfide engineering. *FEBS Lett.* **2014**, *588*, 206–212.
- (40) Craig, D. B.; Dombkowski, A. A. Disulfide by design 2.0: a web-based tool for disulfide engineering in proteins. *BMC Bioinformatics* **2013**, *14*, 346.

- (41) Qian, W.; Krimm, S. Energetics of the disulfide bridge: an ab initio study. *Biopolymers* **1993**, *33* (10), 1591–1603.
- (42) Siegbahn, P. E. M.; Borowski, T. Modeling Enzymatic Reactions Involving Transition Metals. *Acc. Chem. Res.* **2006**, *39* (10), 729–738.
- (43) Stipanuk, M. H. Sulfur amino acid metabolism: pathways for production and removal of homocysteine and cysteine. *Annu. Rev. Nutr.* **2004**, *24*, 539–77.
- (44) Joseph, C. A.; Maroney, M. J. Cysteine dioxygenase: structure and mechanism. *Chem. Commun.* **2007**, 3338–3349.
- (45) Kepenekian, M.; Calborean, A.; Vetere, V.; Le Guennic, B.; Robert, V.; Maldivi, P. Toward Reliable DFT Investigations of Mn-Porphyrins through CASPT2/DFT Comparison. *J. Chem. Theory Comput.* **2011**, *7* (11), 3532–3539.
- (46) *Advanced Inorganic Chemistry*, 6th ed.; Cotton, F. A., Wilkinson, G., Eds.; Wiley–Interscience: New York, 1999.
- (47) Sahu, S.; Goldberg, D. P. Activation of Dioxygen by Iron and Manganese Complexes: A Heme and Nonheme Perspective. *J. Am. Chem. Soc.* **2016**, *138* (36), 11410–11428.
- (48) Nehru, K.; Kim, S. J.; Kim, I. Y.; Seo, M. S.; Kim, Y.; Kim, S. J.; Kim, J.; Nam, W. A highly efficient non-heme manganese complex in oxygenation reactions. *Chem. Commun.* **2007**, *44*, 4623–5.
- (49) Miao, C.; Li, X.; Lee, Y.; Xia, C.; Wang, Y.; Nam, W.; Sun, W. Manganese complex-catalyzed oxidation and oxidative kinetic resolution of secondary alcohols by hydrogen peroxide. *Chem. Sci.* **2017**, *8*, 7476.